Switchable Adhesion via Subsurface Pressure Modulation

Amir Mohammadi Nasab,[†,‡,§] *Aoyi Luo,*[†,#] *Siavash Sharifi,*[§,‖] *Kevin T. Turner,*[*,#] *and Wanliang Shan*[*,§,‖]

[§] Mechanical Engineering Department, University of Nevada, Reno, 1664 N. Virginia Street, Reno, Nevada 89557, USA.

[#] Department of Mechanical Engineering and Applied Mechanics, University of Pennsylvania, 220 South 33rd Street, Philadelphia, Pennsylvania 19104, USA.

[‖] Department of Mechanical and Aerospace Engineering, Syracuse University, Syracuse, NY 13244, USA.

KEYWORDS: dry adhesives, switchable adhesion, subsurface pressure modulation, finite element analysis, mechanics modeling.

ABSTRACT: Materials and devices with tunable dry adhesion have many applications, including transfer printing, climbing robots, and gripping in pick-and-place processes. In this paper, a novel soft device to achieve dynamically tunable dry adhesion via modulation of sub-surface pneumatic pressure is introduced. Specifically, a cylindrical elastomer pillar with a mushroom-shaped cap and annular chamber that can be pressurized to tune the adhesion is investigated. Finite element-

based mechanics models and experiments are used to design, understand, and demonstrate the adhesion of the device. Specifically, the device is designed using mechanics modelling such that the pressure applied inside the annular chamber significantly alters the stress distribution at the adhered interface and thus changes the effective adhesion strength. Devices made of polydimethylsiloxane (PDMS) with different elastic moduli were tested against glass, silicon, and aluminum substrates. Adhesion strengths (σ_0) ranging from ~37 kPa (between PDMS and glass) to ~67 kPa (between PDMS and polished aluminum) are achieved for the unpressurized state. For all cases, regardless of the material and roughness of the substrates, the adhesion strength dropped to 40% of the strength of the unpressurized state (equivalent to a 2.5× adhesion switching ratio) by increasing the chamber pressure from $0.3\sigma_0$ to $0.6\sigma_0$. Furthermore, the strength drops to 20% of the unpressurized strength (equivalent to a 5× adhesion switching ratio) when the chamber pressure is increased to σ_0.

1. Introduction

Devices and materials with dynamically tunable adhesive surfaces that can reversibly switch between "strong" and "weak" adhesion states in response to external stimuli are important in many applications, including wearable devices/electronics, micro transfer printing, climbing robots, and gripping in pick-and-place operations.[1–10] Dry adhesion that relies on van der Waals force has been widely exploited in systems with tunable adhesion due to its versatility and repeatability. Various approaches to alter the dry adhesion strength of an interface have been developed, including mechanical,[11–18] electromagnetic,[19–22] thermal[23–25] and wet-responsive[26] methods.

Here we investigate the use of subsurface pressure modulation for tuning the effective strength of a dry adhesion mediated contact. Subsurface pressure modulation has several advantages

compared to approaches noted above, including versatility (i.e., requires no modification of the adhesive interface), fast actuation (on the order of seconds[27]), and compatibility with a range of environments. Moreover, pneumatically-switchable soft adhesive structures can readily be fabricated using techniques developed for soft robotics and can be seamlessly integrated into soft robotic systems for applications such as robotic grasping. To date, inflatable membranes have been the main approach explored for using subsurface pressure to modulate the behavior of dry adhesive contacts. In the membrane-based approaches, positive pressure is applied to inflate the membrane and reduce the effective adhesion.[4,28–30] Though large adhesion switching ratios can be achieved (e.g., Carlson et al.[4] reported ~50× and Denning et al.[29] reported ~10×), the load capacity of these devices is relatively low. The load capacity is limited by poor distribution of load across the membrane – i.e., the stresses are highest near the circumference of the bonded area and the contact separates via a peeling-dominated failure. Lópeza and Williams[30] studied the adhesion of an elastomeric layer with embedded subsurface microfluidic channels. As pneumatic pressure was applied, the channels were inflated similar to a membrane and ~10× adhesion switching ratio was observed. In other work, it was observed that simply filling subsurface microfluidic channels with air/liquid without further pressurization could also result in enhanced adhesion in a peel test.[31,32] Song and Sitti[33] integrated mushroom-shaped fibrillar adhesives onto a membrane to enhance the adhesion. However, the max adhesion strength achieved was 2 kPa, about 3.6% of the adhesion strength of the same fibrillar adhesives supported by a rigid backing. Song et al.[16] developed a device where a soft, deformable supporting chamber is connected to the membrane. When negative pressure is applied to this device, the negative pressure improves the load distribution and results in enhanced adhesion.

Here, we introduce a novel approach for dynamic dry adhesion tuning through subsurface pressure modulation (SPM). We designed, fabricated, and characterized an elastomer mushroom-shaped structure with an embedded pneumatic chamber (Figure 1). Due to the geometry of the device, the dry adhesion strength in the unpressurized state is relatively high. Pressurization of the annular chamber, which can be done quickly, alters the stress distribution at the interface and reduces the effective adhesion strength (Figure 1). Finite element analysis (FEA) and experiments were conducted to design and investigate the performance of the device. The dry adhesion strength of this SPM device against different types of substrates was characterized as a function of chamber pressure.

2. Materials and methods

2.1 Device Geometry

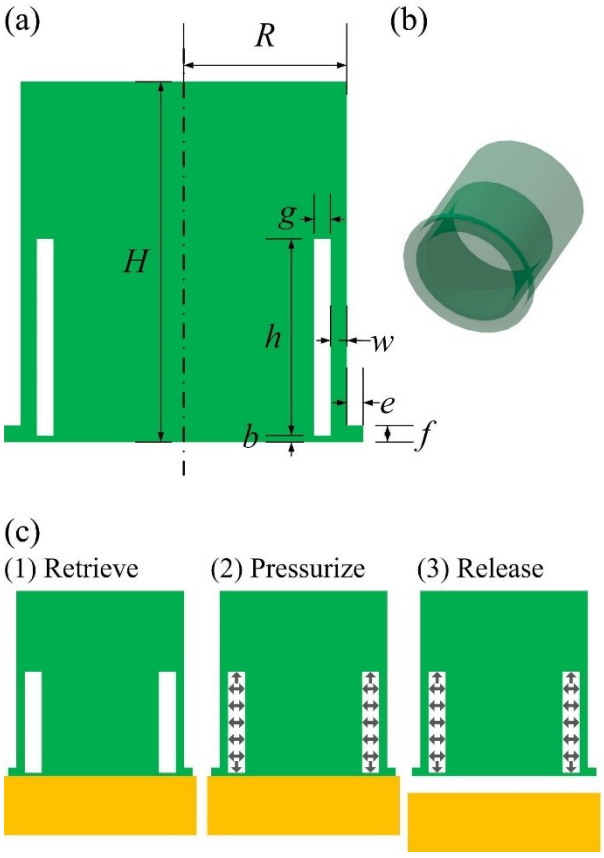

Figure 1. (a) 2D schematic of the device with key design variables labeled. (b) 3D Schematic of the device. (c) Principle of operation. Objects are (1) retrieved in the high-adhesion state (non-pressurized state). (2) Application of internal pressure reduces the adhesion strength by altering the stress distribution at the interface, thus causing (3) the release of the object.

Figure 1 provides an overview of the geometry of the device and its operating principle. Figure 1a shows a schematic of the cross section of the axisymmetric device with key design variables labeled while Figure 1b shows a 3D view. A port (not shown in the schematic) that connects the chamber to an external pressure source is present on the top. Figure 1c demonstrates the basic principle of operation – objects can be retrieved in the "high" adhesion unpressurized state and are released by reducing the effective adhesion through pressurization of the chamber.

The axisymmetric device has overall dimensions of H=10 mm and R=5 mm. The height of the chamber is h=6 mm. The width of the chamber (g), the width of the wall (w), the width of the cap overhang (e) and the height of the cap (f) are all 500±50 μm. The thickness of the bottom layer (b) is varied from 150 μm to 700 μm. The effect of each of these variables on performance of the device is addressed below in modeling and experiments.

2.2 Experiments

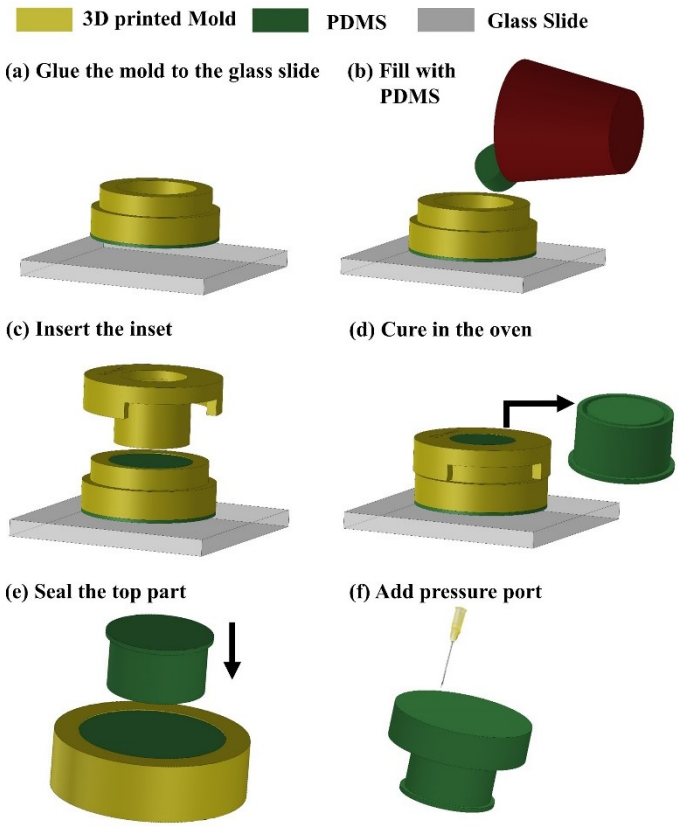

Figure 2. Process used to fabricate the pressure-controlled adhesion structure. (a) A 3D printed mold is bonded to a glass slide. (b) The mold is filled with PDMS. (c) An insert mold is used to form the chamber. Round flanges are designed on the top inset such that it can hold tight to the bottom mold, keeping the inset centered when the two parts are fit together. (d) PDMS is cured in an oven and then removed from the mold. (e) A separate top cap is molded and then bonded to the PDMS section containing the chamber using a thin layer of uncured PDMS as the bonding agent. (f) A pressure port is inserted in the top of the device to connect the chamber to a pressure source.

Device fabrication. The samples were fabricated from polydimethylsiloxane (PDMS) through a multi-step casting and curing process (Figure 2). The three different molds were fabricated by the 3D printing Verowhite^{TM} material (Objet24, Stratasys Inc.) with a glossy finish. The surface roughness of the molds printed with Objet24 with a glossy finish are reported to be R_a=1.915 μm.[34]

PDMS (Sylgard 184, Dow Corning Corporation, Midland, MI), with a 10:1 weight ratio of base elastomer to curing agent, was mixed in a Thinky Mixer (AR-100, THINKY Inc.) for 5 mins and then degassed in a vacuum oven (Across International, AccuTemp) for 15 mins. The first mold was glued to a glass slide (Figure 2a) with half-cured PDMS and was cured in the oven for 30 minutes to ensure good sealing and bonding between the mold and the glass. All of the molds were treated with a mold release agent (Ease release 200, Mann Release Technologies Inc.). The first mold was filled with PDMS (Figure 2b) and the second mold was inserted into the first mold from the top to form the concentric chamber structure (Figure 2c). Round flanges are designed on the top inset such that it can hold tight to the bottom mold, keeping the inset centered when the two parts are fit together. The PDMS was cured in an oven for either 1 or 2 hours at 90 °C; the different cure times yield PDMS with different elastic moduli.[35,36] The cured part was removed from the mold and bonded to a PDMS cap that was molded separately (Figure 2e) in order to seal the chamber. A thin layer of uncured PDMS was used as the bonding agent between the top and bottom part of the device. After curing in the oven for one hour at 90 °C, the complete elastomer structure was removed from the last mold (Figure 2f). A needle is inserted through the cap to connect the chamber to a pneumatic pressure source. Note that several variants of the first mold used in the process were made and used to fabricate PDMS devices with different membrane thicknesses (i.e. *b* in Figure 1b).

Adhesion measurements. The adhesion strengths of the devices were characterized via tests on a universal testing machine (Model 5969, Instron Corp.) equipped with a load cell with a full-scale range of 50 N. The adhesion strength of the devices to various flat substrates, including glass, a silicon wafer, aluminum and polished aluminum, was measured as a function of chamber pressure (0 to 120 kPa). The substrate was fixed to a stage on the bottom of the test frame. A 3D-printed

fixture was used to mount the device on the load cell on the top of the testing frame. This fixture was glued to the top of the device using half-cured PDMS. The bottom surface of the device was aligned to be parallel with the substrate. In a typical adhesion experiment, the device was brought into contact with the substrate at a speed of 50 μm/s until a compressive preload of 9 N (~95 kPa) was reached. The device was held at this preload for 20 seconds and then it was pressurized. After holding the preloaded device in the pressurized state for another 10 seconds it was retracted from the substrate at a speed of 100 μm/s. The adhesion force is defined as the maximum force measured during retraction (i.e. pull-off force). Figure 3 shows a typical force-displacement curve. To identify the failure mechanisms at the interface, the crack initiation and propagation processes during device detachment from a glass slide were imaged using a digital camera. The camera was placed under the glass slide looking perpendicularly at the interface between the device and the glass slide.

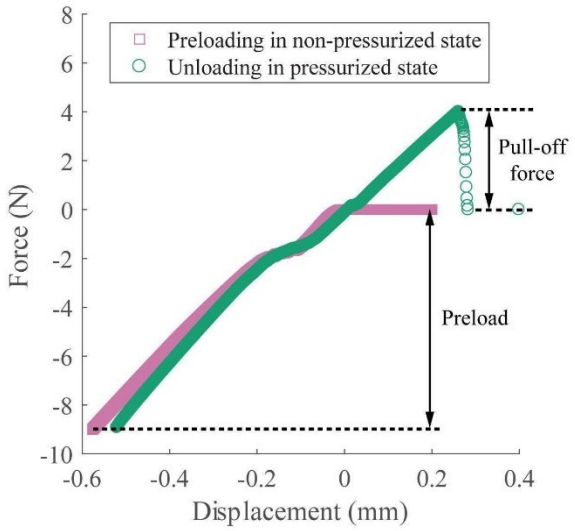

Figure 3. Typical force–displacement curve for adhesion tests. The experimental data is for a device with b=0.22 mm, tested against a glass substrate and actuated with 25 kPa pressure in the chamber.

2.3 Mechanics modelling

The mechanics and design of the device was investigated via a 2D axisymmetric FEA performed using the commercial software Abaqus Standard (Abaqus 2016, Providence, RI). Specifically, the model was used to investigate the stress distribution at the adhered interface as a function of applied normal force on the device and pressure in the internal chamber. The dimensions of the 2D model matched the dimensions of the experimentally fabricated device. The PDMS was modelled as linear elastic material with a Young's modulus of E= 2 MPa and Poisson's ratio v= 0.49. The simulations were conducted under the assumption of small deformations and linear elasticity, thus the overall loading can be decomposed into three different components based on the principle of linear superposition. The use of linear superposition allows the design of the device to be understood with a relatively small number of simulations as the results of each component simulation can be scaled and combined to understand a broad range of cases. Three component simulations with different boundary conditions were completed: 1) Applied normal force: the bottom surface was fixed, and the top surface was displaced uniformly in the z-direction (Figure 4a). 2) Applied sidewall pressure component (Figure 4b), in which uniform pressure is applied to the sidewalls of the chamber. 3) Applied pressure on the top and bottom of the chamber (Figure 4c). The loading in cases 2) and 3) are connected and both are induced when the chamber is pressurized, however the pressurization on the top and side walls of the device was separated in the simulations to provide insight into the mechanics of the device. In all simulations, the distribution of normal stresses along the interface is calculated and extracted with example stress

distributions shown in the bottom row of Figure 4. Results are presented in normalized form: the stresses in the applied load case are normalized by the average stress at the adhered interface (i.e. applied load divided by contact area, F/A_b). The normal stress distribution for the applied pressure component is normalized by the magnitude of applied pressure. Such normalization is chosen to facilitate comparison between our pneumatic devices and conventional vacuum grippers where a unit vacuum pressure generates a unit clamping pressure at the interface. In all cases, there is a stress concentration at the edge and the stress is singular with the form $\sigma=Kd^n$, where K is the magnitude of singularity and depends on the loading condition, d is the distance from the edge and n is an exponent that is negative.[37] Although the exact stress values on the edge of the device are sensitive to the mesh size due to the presence of a singularity, the FEA results can be used to qualitatively compare the stress level of the devices with different geometries as the mesh size is the same for all the simulations.

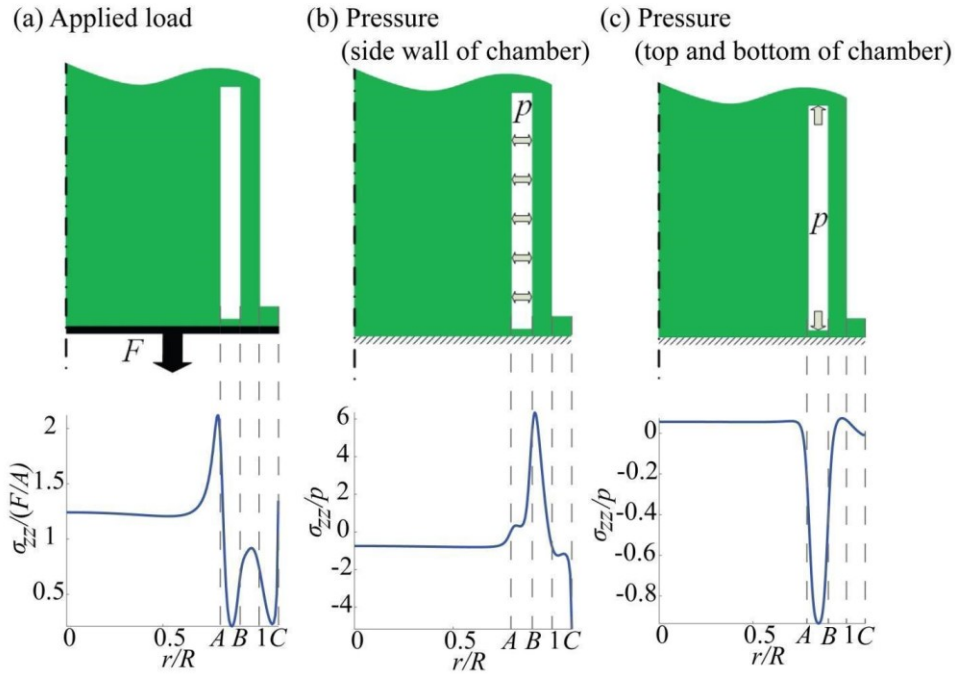

Figure 4. Distribution of normal stress at the adhered interface obtained from FEA with (a) load applied on the adhered interface, (b) pressure applied on the side walls of the chamber, (c) pressure applied on top and bottom walls of the chamber.

3. Results and Discussion

The stress distribution across the interface is critical in determining the effective adhesion strength of an adhered contact. The effective adhesion strength is defined as the pull-off force (i.e. load capacity) of the contact divided by the nominal contact area. Generally, maximum adhesion strength is achieved with a uniform interfacial stress distribution,[38] while any localized stress concentration facilitates crack initiation and reduces the adhesion strength. The goal in designing the current device was thus to achieve: 1) As uniform of a stress distribution in the non-pressurized state to achieve high adhesion strength and 2) A localized high stress concentration when the chamber is pressurized to achieve high tunability.

Figure 4 summarizes the normal stress distribution from each loading component for a device with a bottom layer thickness b=200 μm. The stress distribution shown in Figure 4 is independent of the modulus of the material. For the applied load case (Figure 4a), three local stress maxima are observed in the stress distribution: one is located underneath the edge of the center post (point A), the second one is located underneath the thin wall of the chamber; and the third one is on the edge of the cap, which is a stress singularity point (point C). In all experiments we observed that delamination initiated from the edge of the cap (point C) in the non-pressurized state. Thus, the stress level at the edge of the device (point C) is critical in determining the adhesion strength of the device in the non-pressurized state as widely observed in studies related to fibrillar adhesives. Note, the cap was included in the design to reduce the strength of the singularity at the edge, similar to the concept exploited in "mushroom" shaped fibrillar adhesives.[37,39–43] As noted above,

delamination still initiates at the edge in the unpressurized state even with the cap, however the inclusion of the cap does reduce the strength of the edge singularity and result in increased adhesion strength compared to a device without a cap.

Application of pressure on the sidewalls of the chamber (Figure 4b), results in a high stress at point B and a compressive stress at point C. This is because the thin concentric outer wall is deformed outward and the pressure acting on the wall creates a bending moment that must be balanced by stresses at the interface. Application of pressure on the bottom and top surfaces of the chamber (Figure 4c) results in a compressive stress at the interface below the chamber, and by equilibrium, a smaller tensile stress over the rest of the interface. By comparing the stress values in Fig 4b and 4c, it is evident that the interface stress generated by applying pressure to the bottom and top surfaces of the chamber is much lower than the interface stress resulting from pressure applied to the sidewalls of the chamber. This is significant in device design as it indicates that the stress concentration at the adhered interface and adhesion tunability primarily comes from the pressure on the sidewalls of the chamber and that the geometry should be optimized to maximize this effect.

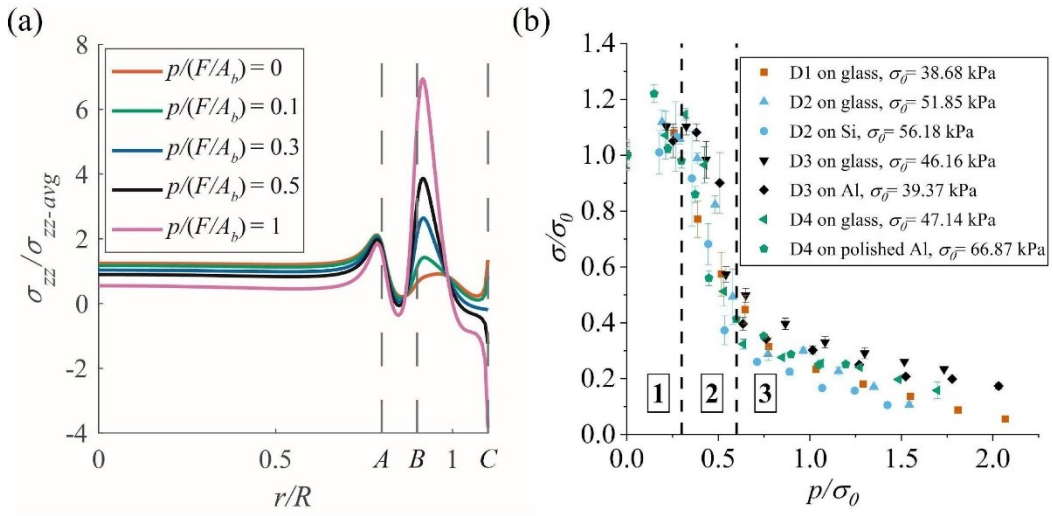

Figure 5. (a) Normalized normal stress distribution with different chamber pressures applied relative to the applied load (F/A_b is the average stress generated by load applied) obtained from FEA, (b) Experimental measured pull-off stress (σ) versus the activation pressure (p) for devices with b=0.22 mm, both axes are normalized by pull of strength at non-pressurized state, σ_0, for each test. The plot is divided into three distinct regions: (1) detachment starts at the edge of the device (point C in panel (a)) and a 10 to 15% increase in adhesion is observed by increasing the pressure, (2) the crack initiation site switches to point B (shown in panel (a)) and a sharp drop in the adhesion strength is observed with increasing the pressure, and (3) the adhesion strength continues to decrease but with a smaller slope.

During use, both normal load and pressure are applied to the device and the stress distribution at the interface is a linear combination of the stress distribution of the three loading components shown in Figure 4. As shown in Figure 5a, as the pressure increases relative to the applied load (i.e. $p/(F/A_b)$ increases), a larger peak tensile stress is generated near point B and the normal stress at edge of the device (point C) reduces and changes from tensile to compressive when $p/(F/A_b)>\sim0.3$. Based on the switch in sign of stress at the edge, the site of crack initiation is expected to shift from point C to point B at $p/(F/A_b)>\sim0.3$.

Measurements of adhesion strength as a function of applied pressure for various devices against different substrates are shown in Figure 5a. The devices have different adhesion strengths at zero applied pressure, σ_0, because the contact surfaces and the Young's modulus of the devices varies in the experiments shown. While σ_0 varies across the experiments, the results collapse to a single curve when the pressure (p) and the adhesion strength (σ) are normalized by σ_0. This shows that the devices with the same dimensions have the same dynamic dry adhesion tunability, and the tunability is independent of overall adhesion strength of the device. The independence of the

adhesion tunability on material modulus and contact surface indicates that this general design is applicable to various materials and substrates, and can be understood by a dimensional analysis as follows. According to linear elastic fracture mechanics, the stress to propagate a crack can be written as $\sigma_f = \sqrt{G_C E/(Y^2 \pi a)}$,[44] where G_c is the critical energy release rate, E is the material modulus, Y is a geometric factor, and a is the crack length. Based on linear superposition discussed above, the normal stress at point i is the sum of the stress generated by the load (σ) and the pressure (p) at point i: $\sigma_i(r_i)=S_p(r_i)\times p+S_\sigma(r_i)\times\sigma$, where $S_p(r_i)$ is the normal stress at point i generated by unit pressure applied and $S_\sigma(r_i)$ is the normal stress at point i generated by unit normal stress applied as shown in Figure 4. The device fails at point i when σ_i reaches the failure stress:

$$S_p(r_i)p + S_\sigma(r_i)\sigma = \sqrt{\frac{G_c E}{Y_i^2 \pi a_i}} \tag{1}$$

where Y_i is the geometric factor for the crack at point i and a_i is the crack length at point i. At non-pressurized state, $p=0$ and all devices are observed to failure from edge (point C) in Figure 4, thus

$$\sigma_0 = \frac{1}{S_\sigma(R)}\sqrt{\frac{G_c E}{Y_R^2 \pi a_R}} \tag{2}$$

where Y_R is the geometric factor for the edge crack (point C) and a_R is the edge crack length (point C). Normalizing eq. (1) by σ_0 in eq. (2) yields:

$$\frac{S_p(r_i)}{S_\sigma(R)}\frac{p}{\sigma_0} + \frac{S_\sigma(r_i)}{S_\sigma(R)}\frac{\sigma}{\sigma_0} = \frac{Y_R}{Y_i}\sqrt{\frac{a_R}{a_i}} \tag{3}$$

Since the geometries of the devices are designed to be the same, $S_p(r_i)/S_\sigma(R)$, $S_\sigma(r_i)/S_\sigma(R)$, and Y_R/Y_i are constant. Assuming a uniform roughness across the substrate, a_R/a_i would also be a constant. As a result of the discussion above, the normalized adhesion strength (σ/σ_0) as a function

of normalized pressure applied (p/σ_0) is independent of the moduli of the device and the substrate tested against.

The adhesion as a function of the applied pressure can be divided into three distinct regions as shown in Figure 5b in which the measured pull-off strength (σ) and the pressure applied to the device (p) are normalized by the adhesion strength of the device in the non-pressurized state (σ_0). In the first region, where the pressure of the chamber is increased from zero up to ~$0.3\sigma_0$, detachment was observed in the experiments to initiate at the edge of the device (point C). As the pressure is increased, the stress at the edge decreases as shown in Figure 5a and can be interpreted from eq. (3), resulting in a 10 to 15% increase in the adhesion strength at p=~$0.3\sigma_0$ compared to the unpressurized state (Figure 5b). In the second region, ~$0.3\sigma_0$<p<~$0.6\sigma_0$, the site where detachment initiates switches to point B and a sharp drop in the adhesion strength (~$0.6\sigma_0$) is observed with increasing pressure. This occurs because the stress at edge (point C) is compressive and there is a sharp increase in the local peak stress at the interface at point B under the chamber (Figure 5a). In the third region, where the chamber pressure is increased above ~$0.6\sigma_0$, the adhesion strength continues to decrease but with a smaller slope. This happens even though the stress at point B is increasing with increasing pressure because the adhesion in the central region of the post provides a floor on the minimum adhesion. Supplemental videos S1 and S2 show the interfacial failure at the edge and at point B, respectively. The effect of applying negative pressure on the adhesion strength of the device was also explored experimentally. Results show that the adhesion strength decreases slightly as negative pressure is applied (Figure S1).

As noted above, the unpressurized adhesion strength, σ_0, varies across the experiments presented in Figure 5b. According to eq. (2), σ_0 scales with $\sqrt{G_C E/a}$, so there are two reasons for the variation of σ_0 in experiments. First, the contact surfaces vary across the experiments and the surface

chemistry and roughness of the surfaces will affect the critical energy release rate (G_c) and the crack length (a) of the interfaces. Notably, increased roughness will result in larger a and thus a lower adhesion strength. For example, for D3 in Figure 5b, the Al surface has a higher roughness than the glass and σ_0 is lower. Second, the cure time of the PDMS was varied for different devices and cure time affects the Young's modulus (E) of PDMS. Realizing that the compliance of the sample (C) is inversely proportional to E and that the contact area (A) is fixed in the current experiments, the force capacity is expected to be proportional to $\sqrt{G_C A/C}$ as reported in previous work.[2] All of the devices were tested on glass and the σ_0 ranges from ~39 to ~51 kPa across the experiments on glass. Sample D4 is over-cured in the oven for two hours in step d of the fabrication process (Figure 2). The experimental results show that the total compliance of D4 is 46.18 (μm/N) whereas that of a regular device (D1) is 61.70 (μm/N). The compliance of the testing system and the 3D printed fixtures is deducted from the compliance of the whole system to find the compliance values of the soft structures. The average adhesion strength at the non-pressurized state for these two devices are σ_{0D4}=47.14 kPa and σ_{0D1}=38.68 kPa, showing a 22% increase for D4 in comparison with D1. These two samples have the same dimensions, and specifically the same sealing layer thickness. Notably, though all the devices tested in this paper have the same overall dimensions (H=10 mm and R=5 mm), the adhesion strength is expected to increase as the device becomes smaller. As the size of the device is reduced, it can better conform to the surface roughness and tends to have smaller fabrication defects, so the defect size is thus expected to scale with overall radius R. As a result, based on eq. (2), σ_0 is expected to scale with $\sqrt{G_C E/R}$ as widely reported by other studies.[18,37,45–47]

To investigate the effect of the geometry on the performance of the device, a parametric study is conducted. The effect of the thickness of the bottom layer (b) is studied through FEA and the

results are summarized in Figure 6a and 6b. The thickness, b, was varied from 0.1 to 0.5 mm (b/R=0.02 to 0.1) in the simulations. For the applied normal loading case (Figure 6a), as the bottom layer becomes thinner, the stress at the edge (point C) decreases while the stress beneath the edge of the center post (point A) increases, thus we expect the adhesion strength to increase if the crack initiates from the edge. However, if the bottom layer is too thin, we expect the site of crack initiation will shift to point A, similar to a mushroom-shaped pillar[37,39,41] and thus the adhesion strength will decrease for thinner bottom layers. When the chamber is pressurized (Figure 6b), a larger tensile stress is generated at point B and a larger compressive stress is generated at point C for the devices with thinner bottom layer since the moment exerted by pressure on thin wall is more strongly transferred to adhered interface. This indicates that the devices with thinner bottom layer are more sensitive to pressure change and both the first and second regions in Figure 5b will be narrower. To verify the trends observed in simulations, devices with different bottom layer thicknesses were fabricated and tested. The results in Figure 7a show the effect of bottom layer thickness on tunability; as the thickness of the bottom layer is reduced, both the first and second regions in Figure 5b are narrower and thus the device has higher tunability. However, in the experiments, cracks were observed to initiate at the edge for all the devices tested in the non-pressurized state and the overall adhesion decreases with thinner bottom layer, which contradicts the prediction of the simulation. This difference is believed to be caused by buckling of the outer wall during the compressive preloading step, since the simulations only consider the pull-off process and the buckling of the outer ring wall during preload is not considered.

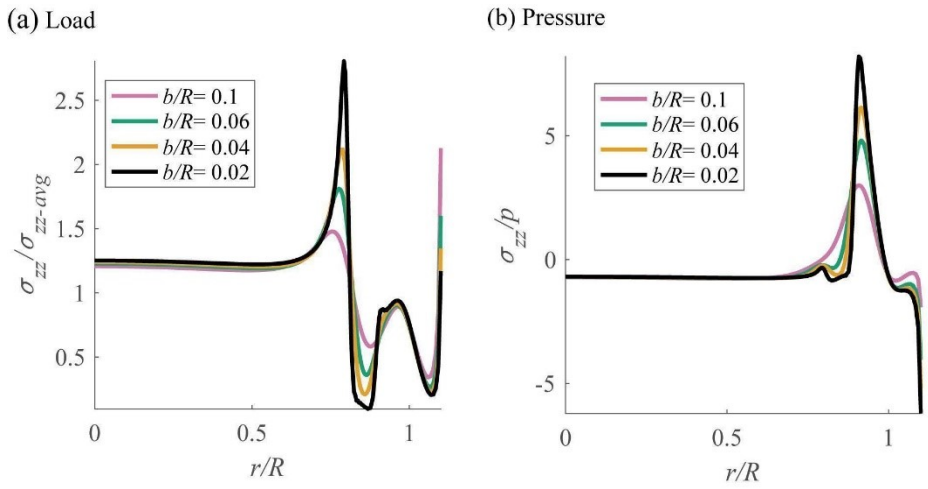

Figure 6. Parametric study of the effect of the thickness of the bottom layer on the stress distribution at the adhered interface when (a) load and (b) pressure are applied obtained from FEA.

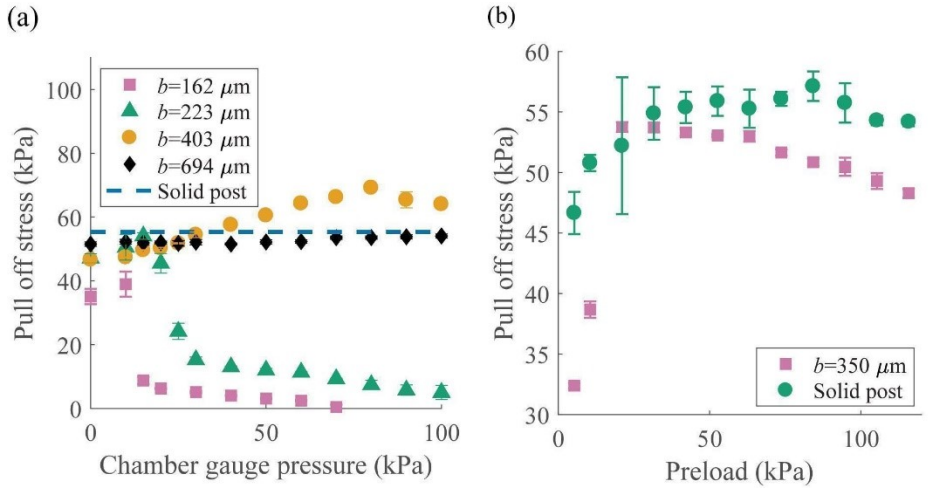

Figure 7. (a) Experimentally measured pull-off stress as a function of chamber pressure for devices with different bottom layer thickness, (b) Experimentally measured pull-off stress versus preload for two devices, one with b=0.35 mm and one solid post, which is a device that has a mushroom-shaped cap but no chamber.

It is widely observed that a compressive overload will cause fibrillar adhesives to buckle. Buckling of the fiber results in local delamination and thus leads to reduced adhesion. Since the

outer wall of our device is a similar slender structure (with aspect ratio of 12), it is expected to buckle similarly under high enough preload. Figure 7b shows the effect of the preload on the adhesion strength of a device with a thin bottom layer (b=0.35 mm) compared to a solid post with no chamber in it. The adhesion strength of the solid post increases with the preload and plateaus at sufficiently large preloads. In comparison, the adhesion strength of the device with a thin bottom layer thickness first increases as the preload increases; this is expected since larger preload results in better contact. Further increase of the preload leads to buckling of the outer ring wall and lower the dry adhesion. The maximum pull-off stress was observed at a preload of 21 kPa. We note that this preload is close to the kink in the load-displacement plot in Figure 2 at ~1.7 N (= 20 kPa), which we believe corresponds to buckling of the sidewall of the device. This behavior is similar to the behavior of fibrillar adhesives under high enough preload and confirms that buckling reduces the adhesion of the device. Since the preload is fixed at 95 kPa for all the tests in Figure 7a, it is expected that the outer ring wall buckles during preload for all the devices with an embedded chamber. As the bottom layer thickness decreases, the point of rotation of the buckled wall is closer to the adhered interface, which likely results in more significant local delamination underneath the wall, and this is believed to lower the adhesion of devices with thinner bottom layer at the non-pressurized state. Moreover, buckling of the wall may also cause the crack to initiate from the edge even for devices with a thin bottom layer, since the delamination region underneath the wall serves as a precrack during pull-off.

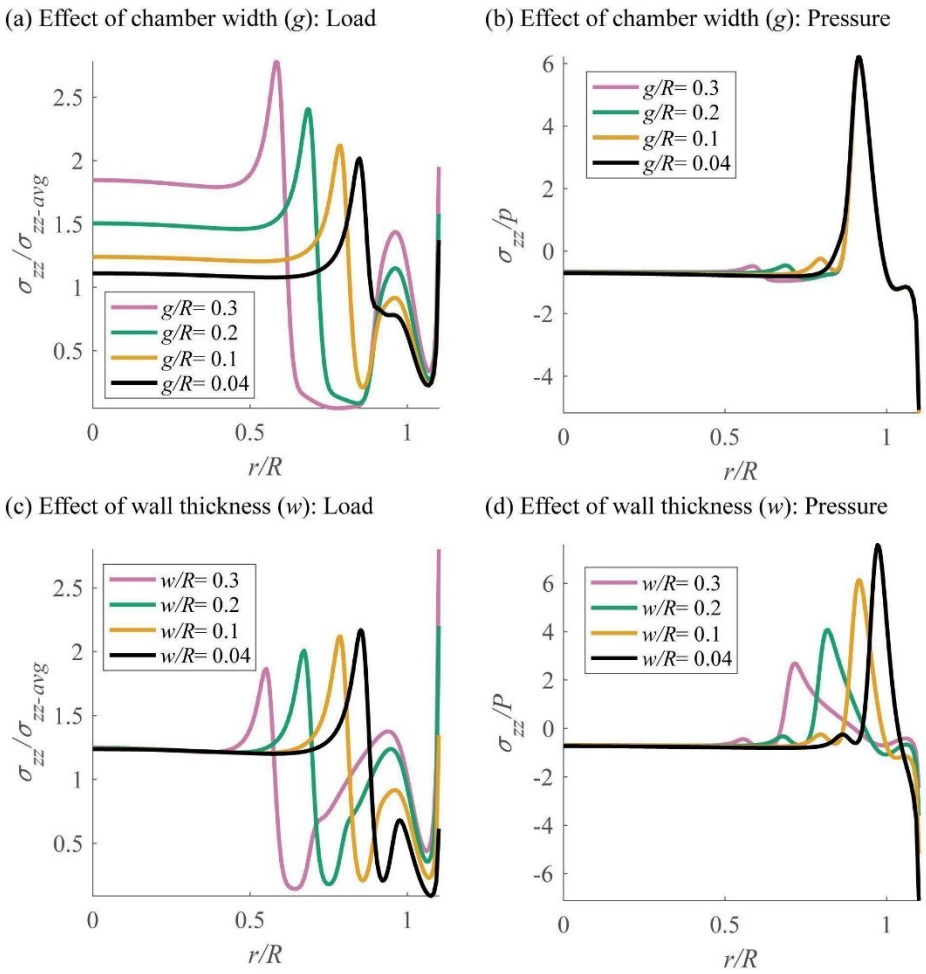

Figure 8. Simulation results of parametric study of the effect of chamber width (a and b) and wall thickness (c and d) on the stress distribution at the adhered interface when a load (a and c) or a pressure (b and d) is applied.

Figure 8a and 8b show the effect of the chamber width (g) on the normal stress distribution at the adhered interface. When the chamber width increases, the radius of the center post decreases accordingly to keep the width of the outer ring wall (w) and the overall radius of the device constant. For a device with larger chamber width and smaller center post, the stress underneath the center post, outer ring wall and edge all increases in the non-pressurized state since there is less effective area to carry the load. However, increasing the chamber width does not significantly

affect the stress distribution, especially the maximum stress at point *B* when pressure is applied (Figure 8b). The effect of the outer wall (*w*) on the normal stress distribution is investigated with the chamber width (*g*) and the overall radius of the device fixed. Thus, an increase of the wall thickness reduces the radius of the center post accordingly. In the non-pressurized state, the stress at the edge increases with increasing wall thickness (Figure 8c), which will result in a lower σ_0. In the case of applying a pressure inside the chamber, the magnitude of the stress is lower at point B for a device with larger wall thickness, which indicates a lower tunability of the dry adhesion. To summarize the findings from Figure 8, minimizing the chamber width and the width of the outer ring wall can lead to higher load capacity at non-pressurized state and higher tunability with the application of pressure.

Figure 9 summarizes the effect of the width (*e*) and the height (*f*) of the overhang on the stress distribution. In the non-pressurized state (Figure 9a and 9c), the stress at the edge decreases with increasing the width of the cap or by decreasing the height of the cap. This trend observed here agrees with the previous studies of that adhesion of mushroom-shaped fibers.[37] When pressure is applied inside the chamber (Figure 9b and 9d), the peak stress at point B increases slightly by decreasing the cap width or the cap height since the moment generated due to the expansion of the outer ring wall is distributed over a smaller cap. Overall, adding a cap to the device will significantly increase the load capacity in the non-pressurized state, σ_0, and slightly decreases the adhesion tunability due to the applied pneumatic pressure. One device without an overhang cap (i.e. $e=f=0$) was tested experimentally (Figure S2). The adhesion strength of this device in the non-pressurized state is 44% lower than devices with an overhanging cap, which demonstrates the importance of the overhang cap on enhancing the adhesion strength.

To demonstrate the application of this pressure-operated device with tunable dry adhesion in pick-and-place, supplemental video S3 shows that a device with a bottom layer thickness of 0.22 mm can pick up a 106 g mass (average stress on interface of ~11 kPa) and hold it for ~110 s in the non-pressurized state before dropping. However if the weight is held for 20 s in the non-pressurized state and the device is pressurized with 30 kPa, the dead weight drops after 10 s. Supplement video S4 shows that the device can pick up a 56 g weight (~5.8 kPa) and hold it without dropping for more than 10 minutes; after that the device is pressurized with 70 kPa and the weight drops. Supplement video S5 shows that the device picks up a 56 g weight in the non-pressurized state and holds it for 13 s; after that the device is pressurized with 40 kPa and releases the weight in ~4 s. These demonstrations clearly show the concept of dynamically tunable dry adhesion with subsurface pressure modulation.

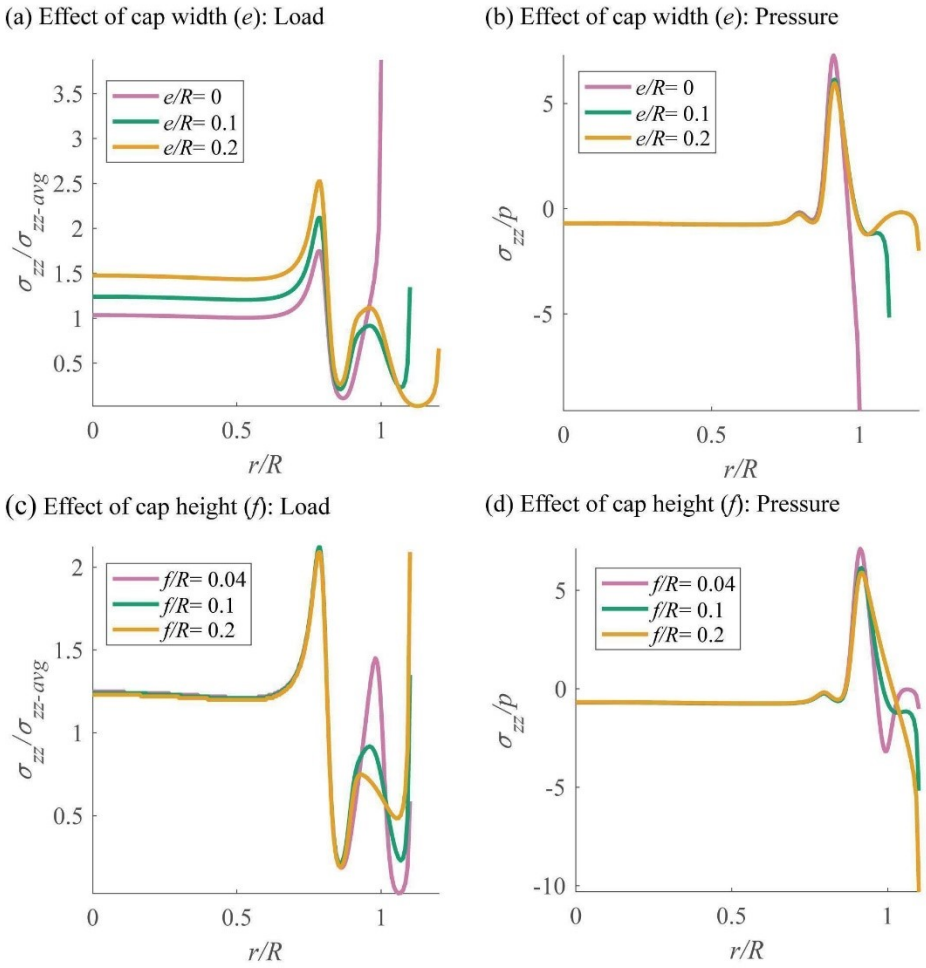

Figure 9. Simulation results of parametric study of the effect of cap width (a and b) and cap height (c and d) on the stress distribution at the adhered interface when a load (a and c) or a pressure (b and d) is applied.

4. Conclusions

An elastomer device with pneumatically tunable dry adhesion through subsurface pressure modulation has been demonstrated. The device consists of an embedded annular chamber near outer side walls of a mushroom-shaped pillar structure. The location and magnitude of the maximum normal stress at the adhered interface and, consequently, the dry adhesion strength is tuned by pressurization of an embedded chamber. Devices made of PDMS with different moduli

were tested against glass, silicon, and aluminum substrates. Adhesion strengths (σ_0) of ~37 (between PDMS and glass) to ~67 kPa (between PDMS and polished aluminum) in the non-pressurized state is achieved. The adhesion strength is reduced to 40% of the strength in the unpressurized state, a 2.5× adhesion switching ratio, by increasing the chamber pressure from $0.3\sigma_0$ to $0.6\sigma_0$, while it decreases to 20% of unpressurized strength, equivalent to a 5× adhesion switching ratio, by increasing the chamber pressure to σ_0. Though the adhesion strength at the non-pressurized state varies, devices with the same dimensions show the same dynamic dry adhesion tunability when normalized. To increase the load capacity of the device and, at the same time, to maximize the dynamic dry adhesion tunability by applying pressure, a parametric study of the mechanics of the device was completed through FEA to optimize the dimensions of the device. The FEA performed in this work focused on understanding the stress distribution at the interface to allow for design of devices with high adhesion strength and high tunability. The FE modeling does not capture more complex phenomena observed in the experiments, such as buckling of the outer wall at high preloads or the complex delamination process after the crack initiates.

ASSOCIATED CONTENT

Supporting Information.

Videos S1-S5

AUTHOR INFORMATION

Corresponding Authors

* E-mail: washan@syr.edu.

* E-mail: kturner@seas.upenn.edu.

Present Addresses

‡ Department of Mechanical Engineering and Materials Science, School of Engineering and Applied Science, Yale University, 9 Hillhouse Ave., New Haven, CT 06511, USA.

Author Contributions

† These authors contributed equally.

The manuscript was written through contributions of all authors. All authors have given approval to the final version of the manuscript.

Notes

The authors declare no competing financial interest.

ACKNOWLEDGMENT

Authors A. Mohammadi Nasab, S. Sharifi, and W. Shan were partially supported by NSF through a CMMI grant 1830388. S. Sharifi and W. Shan were also partially supported by Syracuse Univeristy through startup funds. A. Luo and K. Turner were supported by NSF through CMMI grants 1663037 and 1830475.

REFERENCES

(1) Meitl, M. A.; Zhu, Z. T.; Kumar, V.; Lee, K. J.; Feng, X.; Huang, Y. Y.; Adesida, I.; Nuzzo, R. G.; Rogers, J. A. Transfer Printing by Kinetic Control of Adhesion to an Elastomeric Stamp. *Nat. Mater.* **2006**, *5* (1), 33–38. https://doi.org/10.1038/nmat1532.

(2) Bartlett, M. D.; Croll, A. B.; King, D. R.; Paret, B. M.; Irschick, D. J.; Crosby, A. J. Looking beyond Fibrillar Features to Scale Gecko-like Adhesion. *Adv. Mater.* **2012**, *24* (8), 1078–1083. https://doi.org/10.1002/adma.201104191.

(3) King, D. R.; Bartlett, M. D.; Gilman, C. A.; Irschick, D. J.; Crosby, A. J. Creating Gecko-like Adhesives for "Real World" Surfaces. *Adv. Mater.* **2014**, *26* (25), 4345–4351. https://doi.org/10.1002/adma.201306259.

(4) Carlson, A.; Wang, S.; Elvikis, P.; Ferreira, P. M.; Huang, Y.; Rogers, J. A. Active, Programmable Elastomeric Surfaces with Tunable Adhesion for Deterministic Assembly by Transfer Printing. *Adv. Funct. Mater.* **2012**, *22* (21), 4476–4484. https://doi.org/10.1002/adfm.201201023.

(5) Zhao, R.; Lin, S.; Yuk, H.; Zhao, X. Kirigami Enhances Film Adhesion. *Soft Matter* **2018**, *14* (13), 2515–2525. https://doi.org/10.1039/c7sm02338c.

(6) Drotlef, D. M.; Amjadi, M.; Yunusa, M.; Sitti, M. Bioinspired Composite Microfibers for Skin Adhesion and Signal Amplification of Wearable Sensors. *Adv. Mater.* **2017**, *29* (28), 1701353. https://doi.org/10.1002/adma.201701353.

(7) Feng, X.; Meitl, M. A.; Bowen, A. M.; Huang, Y.; Nuzzo, R. G.; Rogers, J. A. Competing Fracture in Kinetically Controlled Transfer Printing. *Langmuir* **2007**, *23* (25), 12555–12560. https://doi.org/10.1021/la701555n.

(8) Kim-Lee, H. J.; Carlson, A.; Grierson, D. S.; Rogers, J. A.; Turner, K. T. Interface Mechanics of Adhesiveless Microtransfer Printing Processes. *J. Appl. Phys.* **2014**, *115* (14), 143513. https://doi.org/10.1063/1.4870873.

(9) Tatari, M.; Mohammadi Nasab, A.; Turner, K. T.; Shan, W. Dynamically Tunable Dry Adhesion via Subsurface Stiffness Modulation. *Adv. Mater. Interfaces* **2018**, *5* (18), 1800321. https://doi.org/10.1002/admi.201800321.

(10) Alizadehyazdi, V.; Spenko, M. A Microstructured Adhesive Gripper with Piezoelectric Controlled Adhesion, Cleaning, and Sensing. *Smart Mater. Struct.* **2019**, *28* (11), 115037. https://doi.org/10.1088/1361-665X/ab46fc.

(11) Zhao, B.; Pesika, N.; Rosenberg, K.; Tian, Y.; Zeng, H.; McGuiggan, P.; Autumn, K.; Israelachvili, J. Adhesion and Friction Force Coupling of Gecko Setal Arrays: Implications for Structured Adhesive Surfaces. *Langmuir* **2008**, *24* (4), 1517–1524. https://doi.org/10.1021/la702126k.

(12) Zeng, H.; Pesika, N.; Tian, Y.; Zhao, B.; Chen, Y.; Tirrell, M.; Turner, K. L.; Israelachvili, J. N. Frictional Adhesion of Patterned Surfaces and Implications for Gecko and Biomimetic Systems. *Langmuir* **2009**, *25* (13), 7486–7495. https://doi.org/10.1021/la900877h.

(13) Minsky, H. K.; Turner, K. T. Achieving Enhanced and Tunable Adhesion via Composite Posts. *Appl. Phys. Lett.* **2015**, *106* (20), 201604. https://doi.org/10.1063/1.4921423.

(14) Murphy, M. P.; Aksak, B.; Sitti, M. Gecko-Inspired Directional and Controllable Adhesion. *Small* **2009**, *5* (2), 170–175. https://doi.org/10.1002/smll.200801161.

(15) Pang, C.; Kim, S. M.; Rahmawan, Y.; Suh, K. Y. Beetle-Inspired Bidirectional, Asymmetric Interlocking Using Geometry-Tunable Nanohairs. *ACS Appl. Mater. Interfaces* **2012**, *4* (8), 4225–4230. https://doi.org/10.1021/am3009289.

(16) Song, S.; Drotlef, D.-M.; Majidi, C.; Sitti, M. Controllable Load Sharing for Soft Adhesive

Interfaces on Three-Dimensional Surfaces. *Proc. Natl. Acad. Sci.* **2017**, *114* (22), E4344–E4353. https://doi.org/10.1073/pnas.1620344114.

(17) Purtov, J.; Frensemeier, M.; Kroner, E. Switchable Adhesion in Vacuum Using Bio-Inspired Dry Adhesives. *ACS Appl. Mater. Interfaces* **2015**, *7* (43), 24127–24135. https://doi.org/10.1021/acsami.5b07287.

(18) Minsky, H. K.; Turner, K. T. Composite Microposts with High Dry Adhesion Strength. *ACS Appl. Mater. Interfaces* **2017**, *9* (21), 18322–18327. https://doi.org/10.1021/acsami.7b01491.

(19) Drotlef, D. M.; Blümler, P.; Del Campo, A. Magnetically Actuated Patterns for Bioinspired Reversible Adhesion (Dry and Wet). *Adv. Mater.* **2014**, *26* (5), 775–779. https://doi.org/10.1002/adma.201303087.

(20) Northen, M. T.; Greiner, C.; Arzt, E.; Turner, K. L. A Gecko-Inspired Reversible Adhesive. *Adv. Mater.* **2008**, *20* (20), 3905–3909. https://doi.org/10.1002/adma.200801340.

(21) Gillies, A. G.; Kwak, J.; Fearing, R. S. Controllable Particle Adhesion with a Magnetically Actuated Synthetic Gecko Adhesive. *Adv. Funct. Mater.* **2013**, *23* (26), 3256–3261. https://doi.org/10.1002/adfm.201203122.

(22) Linghu, C.; Wang, C.; Cen, N.; Wu, J.; Lai, Z.; Song, J. Rapidly Tunable and Highly Reversible Bio-Inspired Dry Adhesion for Transfer Printing in Air and a Vacuum. *Soft Matter* **2019**, *15*, 30–37. https://doi.org/10.1039/C8SM01996G.

(23) Qu, L.; Dai, L. Gecko-Foot-Mimetic Aligned Single-Walled Carbon Nanotube Dry Adhesives with Unique Electrical and Thermal Properties. *Adv. Mater.* **2007**, *19* (22), 3844–3849. https://doi.org/10.1002/adma.200700023.

(24) Kim, S.; Sitti, M.; Xie, T.; Xiao, X. Reversible Dry Micro-Fibrillar Adhesives with Thermally Controllable Adhesion. *Soft Matter* **2009**, *5* (19), 3689–3693. https://doi.org/10.1039/b909885b.

(25) Keum, H.; Yang, Z.; Han, K.; Handler, D. E.; Nguyen, T. N.; Schutt-Aine, J.; Bahl, G.; Kim, S. Microassembly of Heterogeneous Materials Using Transfer Printing and Thermal Processing. *Sci. Rep.* **2016**, *6* (1), 29925. https://doi.org/10.1038/srep29925.

(26) Yi, H.; Seong, M.; Sun, K.; Hwang, I.; Lee, K.; Cha, C.; Kim, T. Il; Jeong, H. E. Wet-Responsive, Reconfigurable, and Biocompatible Hydrogel Adhesive Films for Transfer Printing of Nanomembranes. *Adv. Funct. Mater.* **2018**, *28* (18), 1706498. https://doi.org/10.1002/adfm.201706498.

(27) Croll, A. B.; Hosseini, N.; Bartlett, M. D. Switchable Adhesives for Multifunctional Interfaces. *Advanced Materials Technologies*. Wiley-Blackwell 2019. https://doi.org/10.1002/admt.201900193.

(28) Arul, E. P.; Ghatak, A. Control of Adhesion via Internally Pressurized Subsurface

Microchannels. *Langmuir* **2012**, *28* (9), 4339–4345. https://doi.org/10.1021/la204618u.

(29) Dening, K.; Heepe, L.; Afferrante, L.; Carbone, G.; Gorb, S. N. Adhesion Control by Inflation: Implications from Biology to Artificial Attachment Device. *Appl. Phys. A Mater. Sci. Process.* **2014**, *116* (2), 567–573. https://doi.org/10.1007/s00339-014-8504-2.

(30) Prieto-López, L. O.; Williams, J. A. Using Microfluidics to Control Soft Adhesion. *J. Adhes. Sci. Technol.* **2016**, *30* (14), 1555–1573. https://doi.org/10.1080/01694243.2016.1155878.

(31) Majumder, A.; Sharma, A.; Ghatak, A. A Bioinspired Wet/Dry Microfluidic Adhesive for Aqueous Environments. *Langmuir* **2010**, *26* (1), 521–525. https://doi.org/10.1021/la9021849.

(32) Visser, T.; Masetto, N.; Wessling, M. Microfluidic Adhesion Induced by Subsurface Microstructures. *Science (80-.).* **2007**, *318* (5848), 258–261. https://doi.org/10.1016/j.memsci.2007.07.048.

(33) Song, S.; Sitti, M. Soft Grippers Using Micro-Fibrillar Adhesives for Transfer Printing. *Adv. Mater.* **2014**, *26* (28), 4901–4906. https://doi.org/10.1002/adma.201400630.

(34) Hwang, Y.; Paydar, O. H.; Candler, R. N. 3D Printed Molds for Non-Planar PDMS Microfluidic Channels. *Sensors Actuators, A Phys.* **2015**, *226*, 137–142. https://doi.org/10.1016/j.sna.2015.02.028.

(35) Seghir, R.; Arscott, S. Extended PDMS Stiffness Range for Flexible Systems. *Sensors Actuators, A Phys.* **2015**, *230*, 33–39. https://doi.org/10.1016/j.sna.2015.04.011.

(36) Nasab, A. M.; Sabzehzar, A.; Tatari, M.; Majidi, C.; Shan, W. A Soft Gripper with Rigidity Tunable Elastomer Strips as Ligaments. *Soft Robot.* **2017**, *4* (4), 411–420. https://doi.org/10.1089/soro.2016.0039.

(37) Balijepalli, R. G.; Begley, M. R.; Fleck, N. A.; McMeeking, R. M.; Arzt, E. Numerical Simulation of the Edge Stress Singularity and the Adhesion Strength for Compliant Mushroom Fibrils Adhered to Rigid Substrates. *Int. J. Solids Struct.* **2016**, *85–86*, 160–171. https://doi.org/10.1016/j.ijsolstr.2016.02.018.

(38) Gao, H.; Yao, H. Shape Insensitive Optimal Adhesion of Nanoscale Fibrillar Structures. *Proc. Natl. Acad. Sci.* **2004**, *101* (21), 7851–7856. https://doi.org/10.1073/pnas.0400757101.

(39) Del Campo, A.; Greiner, C.; Arzt, E. Contact Shape Controls Adhesion of Bioinspired Fibrillar Surfaces. *Langmuir* **2007**, *23* (20), 10235–10243. https://doi.org/10.1021/la7010502.

(40) Carbone, G.; Pierro, E.; Gorb, S. N. Origin of the Superior Adhesive Performance of Mushroom-Shaped Microstructured Surfaces. *Soft Matter* **2011**, *7* (12), 5545–5552. https://doi.org/10.1039/c0sm01482f.

(41) Aksak, B.; Sahin, K.; Sitti, M. The Optimal Shape of Elastomer Mushroom-like Fibers for High and Robust Adhesion. *Beilstein J. Nanotechnol* **2014**, *5*, 630–638. https://doi.org/10.3762/bjnano.5.74.

(42) Spuskanyuk, A. V.; McMeeking, R. M.; Deshpande, V. S.; Arzt, E. The Effect of Shape on the Adhesion of Fibrillar Surfaces. *Acta Biomater.* **2008**, *4*, 1669–1676. https://doi.org/10.1016/j.actbio.2008.05.026.

(43) Carbone, G.; Pierro, E. Sticky Bio-Inspired Micropillars: Finding the Best Shape. *Small* **2012**, *8* (9), 1449–1454. https://doi.org/10.1002/smll.201102021.

(44) Anderson, T. L. *FRACTURE MECHANICS: Fundamentals and Applications*, Fourth Edi.; CRC Press, Taylor & Francis Group, 2017.

(45) Hensel, R.; Moh, K.; Arzt, E. Engineering Micropatterned Dry Adhesives: From Contact Theory to Handling Applications. *Adv. Funct. Mater.* **2018**, *28* (28), 1800865. https://doi.org/10.1002/adfm.201800865.

(46) Balijepalli, R. G.; Fischer, S. C. L.; Hensel, R.; McMeeking, R. M.; Arzt, E. Numerical Study of Adhesion Enhancement by Composite Fibrils with Soft Tip Layers. *J. Mech. Phys. Solids* **2017**, *99*, 357–378. https://doi.org/10.1016/j.jmps.2016.11.017.

(47) Crosby, A. J.; Shull, K. R.; Lakrout, H.; Creton, C. Deformation and Failure Modes of Adhesively Bonded Elastic Layers. *J. Appl. Phys.* **2000**, *88* (5), 2956–2966. https://doi.org/10.1063/1.1288017.

For Table of Contents Only: